Activation of Ultrathin SrTiO3 with Subsurface SrRuO3 for the Oxygen Evolution Reaction

Journal:	*Energy & Environmental Science*
Manuscript ID	EE-ART-01-2018-000210.R1
Article Type:	Paper
Date Submitted by the Author:	09-Mar-2018
Complete List of Authors:	Akbashev, Andrei; Department of Materials Science and Engineering, Stanford University, Stanford, California, 94305, USA; Stanford Institute for Materials and Energy Sciences, SLAC National Accelerator Laboratory, Menlo Park, California, 94025, USA Zhang, Liang; University of Pennsylvania, Chemical and Biomolecular Engineering Mefford, J.; Department of Materials Science and Engineering, Stanford University, Stanford, California, 94305, USA; Stanford Institute for Materials and Energy Sciences, SLAC National Accelerator Laboratory, Menlo Park, California, 94025, USA Park, Junsuk; Department of Materials Science and Engineering, Stanford University, Stanford, California, 94305, USA Butz, Benjamin; Department of Materials Science and Engineering, Stanford University, Stanford, California, 94305, USA; Institut für Werkstofftechnik & Gerätezentrum für Mikro- und Nanoanalytik (MNaF), Universität Siegen, 57068 Siegen, Germany Luftman, Henry; Surface Characterization Facility, Lehigh University, Bethlehem, Pennsylvania, 18105, USA Chueh, William; Department of Materials Science and Engineering, Stanford University, Stanford, California, 94305, USA; Stanford Institute for Materials and Energy Sciences, SLAC National Accelerator Laboratory, Menlo Park, California, 94025, USA Vojvodic, Aleksandra; University of Pennsylvania, Chemical and Biomolecular Engineering

Broader context:

Designing simultaneous activity and stability during electrochemical water splitting is a significant challenge for the development of energy conversion materials. Often, high electrocatalytic activity of oxides is accompanied by structural instability. A core-shell design, where an active core catalyst is covered with a stable shell, is an attractive solution to the problem of catalyst instability. However, the influence of the core during electrocatalytic reactions on the surface of the shell of oxide systems is not well understood. Herein, we demonstrate how ultrathin heterostructures composed of unstable active and stable inactive layers can be used for studies of model core-shell oxide architectures. In particular, we show that as little as an 0.4-nm (1 unit cell) subsurface layer of an active perovskite $SrRuO_3$ "core" can activate a $SrTiO_3$ "shell" surface layer towards oxygen evolution reaction (OER). Importantly, we find that 1 nm (2 unit cells) of the shell layer is enough to completely protect the inherently unstable catalyst against corrosion during the OER. Using density functional theory calculations, we unravel the mechanism for the subsurface activation: Burying an active material under an ultrathin shell layer introduces new electronic states in the heterostructure, enhancing the interaction between the adsorbates and the shell layer.

Energy & Environmental Science

ARTICLE

Activation of Ultrathin $SrTiO_3$ with Subsurface $SrRuO_3$ for the Oxygen Evolution Reaction

Received 00th January 20xx,
Accepted 00th January 20xx

DOI: 10.1039/x0xx00000x

www.rsc.org/

A.R. Akbashev[1,2,*], L. Zhang[3,*], J. Tyler Mefford[1,2], J. Park[1], B. Butz[1,4], H. Luftman[5], W.C. Chueh[1,2,†], A. Vojvodic[3,†]

Water electrolysis occurs via the oxygen/hydrogen evolution reactions.[1,2] Achieving sufficiently high oxygen evolution reaction (OER) activity while maintaining stability of the active catalyst surface is a primary challenge of designing OER catalysts.[1,3] Often high electrocatalytic activity is accompanied by structural instability.[4-6] This is the case for the metallic perovskite oxide $SrRuO_3$ (SRO), which exhibits rapid dissolution under OER conditions, both as thin-films[4] and as nanoparticles.[7] On the other hand, large band-gap perovskite oxides such as $SrTiO_3$ (STO) are inactive for OER in the dark but are stable.[8] In this work, we demonstrate that burying as little as one unit cell of SRO beneath an ultrathin STO capping layer activates the otherwise inert electrocatalyst and gives excellent stability. Using density functional theory (DFT) calculations, we find that such a chemical perturbation of STO by sub-surface SRO introduces new 4*d* electronic states including Ru states within the STO band gap, raising the energy level of the electrons, changing the electronic hybridization, and facilitating an easy transfer to the adsorbed intermediates. We validate this hypothesis experimentally using atomically precise heteroepitaxial deposition. We find that a single-unit-cell layer of SRO is sufficient to activate the topmost STO layer towards OER; burying SRO underneath two unit cells of STO protects the inherently unstable SRO against corrosion during OER. Generally, our layered heterostructures are model systems of oxide core-shell structures, where an unstable catalyst (core) is protected against degradation and electronically activates the otherwise inactive shell.[9] As demonstrated in this work, the growth of ultrathin heterostructures establishes a rigorous platform for screening core/shell nanoparticle combinations/thicknesses, and elucidates sub-surface activation mechanism for achieving stable and active oxide electrocatalysts.

Introduction

Many metal oxides, including perovskite oxides, exhibit deactivation and structural transformation[4,10] during electrolysis, which poses significant challenges for use in water electrolyzers and fuel cells.[6,11] Core-shell nanoparticles with nanometers-thick shells are used as electrocatalysts to improve structural stability and catalytic activity. A plethora of metallic core/shell combinations have been realized with well-controlled size and morphology.[12-16] However, when it comes to oxide-based core-shell structures, the data is scarce due to the challenging syntheses.[9,17,18] Recently, heterogeneous Ir-based perovskite $SrIrO_3$ and pyrochlore $Y_2Ir_2O_7$ catalysts were reported to exhibit exceptionally high OER activity after major surface reconstruction and formation of an OER-active protecting thin-film layer of IrO_x on the original surface.[10,19] Such self-forming heterostructures motivate the investigation of artificial epitaxial metal-oxide heterostructures, which offers diverse cation chemistries and precise thickness control. Naturally, thin films are ideal platforms for understanding design rules for engineering activity and stability, though most model systems studies of single-crystalline oxide films for water electrolysis have been conducted on relatively thick, single-material films (thickness > 10 nm), such as $SrCoO_3$,[20] $SrIrO_3$,[10,21] IrO_2,[22] RuO_2,[22,23] $LaCoO_3$,[24], $SrRuO_3$,[4,25] and $La_{1-x}Sr_xMnO_3$.[26]

1. *Department of Materials Science and Engineering, Stanford University, Stanford, California, 94305, USA*
2. *Stanford Institute for Materials and Energy Sciences, SLAC National Accelerator Laboratory, Menlo Park, California, 94025, USA*
3. *Department of Chemical and Biomolecular Engineering, University of Pennsylvania, Philadelphia, Pennsylvania, 19104, USA*
4. *Institut für Werkstofftechnik & Gerätezentrum für Mikro- und Nanoanalytik (MNaF), Universität Siegen, 57068 Siegen, Germany*
5. *Surface Characterization Facility, Lehigh University, Bethlehem, Pennsylvania, 18105, USA*

* These authors contributed equally to this work

† Correspondence and requests for materials should be addressed to W.C.C (email wchueh@stanford.edu) or to A.V. (email alevoj@seas.upenn.edu)

Electronic Supplementary Information (ESI) available: [details of any supplementary information available should be included here]. See DOI: 10.1039/x0xx00000x

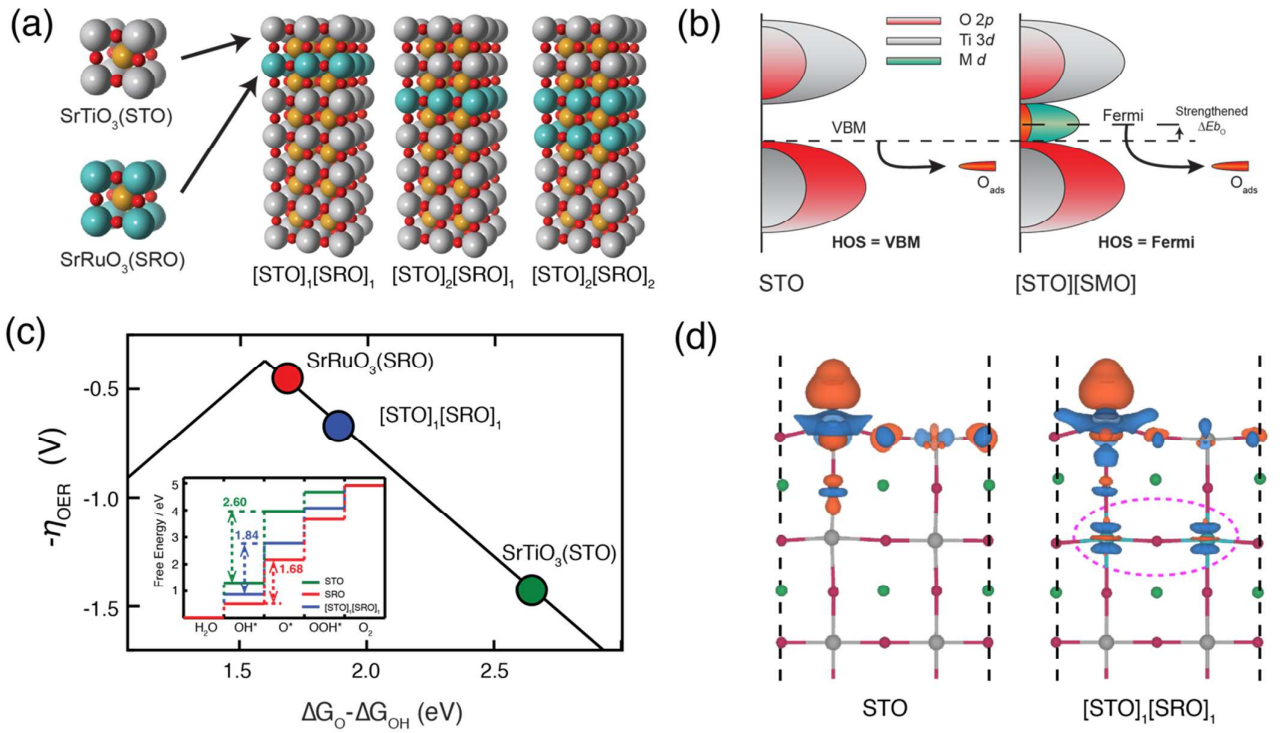

Figure 1. (a) Schematics of the $[STO]_n[SRO]_m$ perovskite heterostructure system design. The top *n* unit cells of STO serve as a protective capping layer, whereas the buried *m* unit cells of SRO activate the top STO surface for OER. (b) Schematic density of states (DOS) illustrating the influence of the buried SRO layer on the interaction between the surface-adsorbed O and the top STO layer. (c) DFT-calculated theoretical OER activity as a function of the standard free energy difference ΔG_O-ΔG_{OH}. The inset shows a calculated standard free energy diagram for the OER on the heterostructures systems including the surfaces of STO (green), SRO (red) and $[STO]_1[SRO]_1$ (blue). Dashed arrows mark the free energy differences of the potential-determining step of these three systems. (d) Calculated differential valence-electron charge densities of O adsorption on $[STO]_1[SRO]_1$ ($\Delta\rho = \rho_{O\text{-}surf} - \rho_{surf} - \rho_O$); charge depletion and accumulation are illustrated by blue and orange regions, respectively (isosurfaces are set to 0.005 e/Å^2).

In this study, we utilize perovskite heterostructures with an ultrathin core-shell-like architecture (component core/shell thicknesses starting from 0.4 nm) as model systems for designing active and stable electrocatalysts. These materials are heterostructured (multilayer) thin films epitaxially grown on a single-crystalline substrate. Figure 1a illustrates these heterostructures, where a highly OER-active $SrRuO_3$ (SRO) layer is buried under a highly stable $SrTiO_3$ (STO) capping layer. On the basis of density functional theory (DFT) calculations, we propose a mechanism for sub-surface electronic activation of these ultrathin oxide heterostructures for OER. Experimentally, we demonstrate that as little as 1 unit cell (u.c.) of SRO activates STO, and as little as 2 u.c. of STO is sufficient to suppress the dissolution of SRO. Our work opens up a new dimension for engineering active and stable oxide electrocatalysts.

Results and discussion

Nominally undoped and Nb-doped STO are poor OER electrocatalysts, the latter introduces electronic conductivity without changing the crystal structure and lattice constants of STO.[8] However, they are stable under high anodic potentials. We therefore propose an ultrathin heterostructure consisting of STO as the host material with a buried $SrMO_3$ (M – transition metal) perovskite layer that could activate the STO capping layer for OER. Although we present these films as model systems for core-shell architectures, it should be noted that the single-layer epitaxial growth of *electrodes* requires the deposition of the core material (SRO) onto an electronically conductive atomically flat lattice-matched substrate (in this case, Nb-doped STO), which serves as a current collector. We first qualitatively discuss the electrocatalytic functionality of this heterostructure, and then present DFT predictions and experimental validations. From an electronic structure perspective, we hypothesize that sub-surface activation occurs when the $SrMO_3$ introduces spatially accessible electronic states inside or in the vicinity of the STO band gap. This is illustrated by the schematic density of states (DOS) plot of an STO surface in Figure 1b, where O adsorption is used as an example. The addition of an appropriately chosen sub-surface guest oxide raises the highest occupied state (HOS) from the valence band maximum (VBM) of the host STO (Figure 1b, left) to the Fermi level, which is pinned by the sub-surface oxide states (Figure 1b, right). Since the surface adsorption of O involves charge transfer from the HOS to the O 2*p* adsorbate

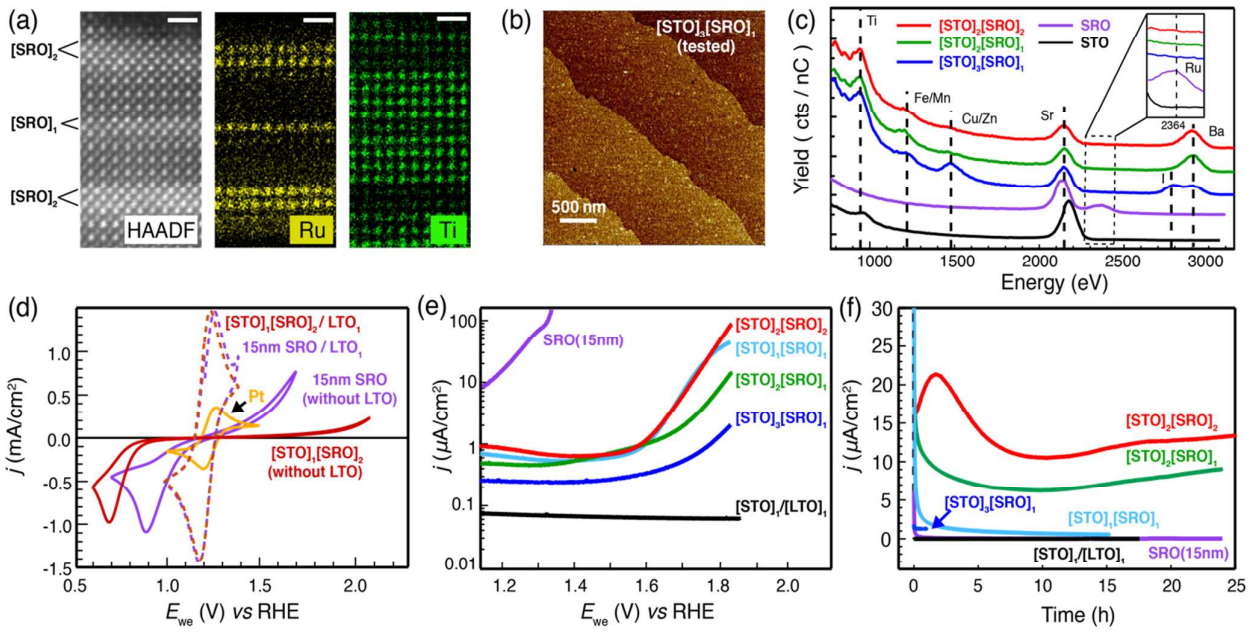

Figure 2. (a) HAADF-STEM image and Ti and Ru EDX maps of a heterostructure containing different $[SRO]_m$ (m=1,2) layers sandwiched between $[STO]_4$ layers. Maps of chemical elements are given for Sr, Ti and Ru. The scale bar is 1 nm. For more information, see Extended Data Figure 10. (b) Atomic force microscopy image of the $[STO]_3[SRO]_1$ heterostructure after OER evaluation. (c) Low-energy ion scattering spectra of the $[STO]_n[SRO]_m$ heterostructures confirms that the topmost surface does not have Ru after 1-24 h testing under overpotential of 1.8 V *vs* RHE. Other elements (Fe/Mn, Cu/Zn, Ba, I) likely originated from the KOH solution. The spectra for pure STO and SRO are given for comparison purposes. The spectrum for STO is slightly shifted to higher energies due to excessive surface charging during spectra collection. (d) Cyclic voltammetry of the $[STO]_1[SRO]_2$ heterostructure and 15-nm SRO film grown with and without a 1-u.c. $LaTiO_3$ layer at the film-substrate interface, as measured in a solution of 0.1 M KOH and 20/20 mM $[Fe(CN)_6]^{3-/4-}$. (e) Tafel plot showing OER activity of the $[STO]_n[SRO]_1$ (n = 1,2,3) and $[STO]_2[SRO]_2$ heterostructures, bare $[STO]_1[LTO]_1/STO_{sub}$ and SRO films. Scan rate is 10 mV/s. (f) Potentiostatic measurements of stability (overpotential is 0.64 V *vs* RHE) for the samples shown in (e). The $[STO]_1[SRO]_1$ sample in (f) utilizes a modified deposition recipe as described in main text. The dashed black line represents the SRO dissolution concurrent with the OER under 0.64 V vs RHE. The solid purple line shows the measured current for SRO after the potential reached 0.64 V vs RHE.

states (O_{ads}), a more energetic HOS stabilizes the adsorbate-surface bond, resulting in enhanced surface reactivity. Other OER intermediates such as OH^* and OOH^* follow the same activation mechanism, but with a smaller enhancement in adsorption.[27] Such an electronic interaction likely persists for no more than few u.c. Similarly, from an electron transport perspective, the electronic interaction between $SrMO_3$ and STO will also increase the carrier concentrations in the STO capping layer. This effect, distinct from two-dimensional doping,[28] which is predominately electrostatic in nature, is again characterized by the short, a few-unit-cell interaction distance. Beyond this length scale, tunneling, defect-mediated transport and space-charge may be operative.[29,30]

Our DFT-calculated DOS of $SrMO_3$ and STO suggest that the Ru 4*d* states of the $SrRuO_3$ sub-surface layer are energetically positioned inside the STO band gap and hybridize with the STO bands (Extended Data Figure 1). We further used DFT to evaluate the theoretical OER overpotential of these ultrathin heterostructures. The following notation is used: $[STO]_n[SRO]_m$, where the heterostructure consists of *n* u.c. of STO on top of *m* u.c. of SRO, both lattice matched to the (001)-oriented STO substrate (Methods). Surface stability Pourbaix diagram (Extended Data Figure 2) shows that formation of lattice oxygen vacancies is not favored at the surface of the $[STO]_1[SRO]_1$ heterostructure under OER conditions. Thus, the oxygen evolution is likely dominated by the adsorbate-mediated pathway rather than by the lattice oxygen pathway.[31,32] We consider the OH^*, O^* and OOH^* intermediates when constructing free energy diagrams of the four consecutive coupled proton-electron transfer steps and calculate the theoretical OER overpotential using ΔG_{O^*}-ΔG_{OH^*} as an OER activity descriptor.[33,34] We demonstrate that pure STO, pure SRO and the $[STO]_1[SRO]_1$ heterostructure (Figure 1c) are all on the right-hand side of the OER activity volcano, where the potential-limiting step is the deprotonation of OH^* to form O^*. Interestingly, the calculated OER overpotential of the $[STO]_1[SRO]_1$ heterostructure (0.61 V) is closer to that of SRO (0.45 V) than of STO (1.36 V). This supports our hypothesis that the surface of the $[STO]_1[SRO]_1$ heterostructure could be active for OER. Figure 1d shows the calculated electron charge density differences induced by the oxygen adsorbed at the surface of STO and $[STO]_1[SRO]_1$ heterostructures ($\Delta\rho = \rho_{O\text{-}surf} - \rho_{surf} - \rho_O$). We see that O adsorbate accepts a similar

number of electrons from the heterostructure (Table 1 in Supplementary Information). However, the key difference between the structures lies in the origin of this charge. For $[STO]_1[SRO]_1$, we find that a charge of 0.17e is donated from the Ru sublayer and transferred via the capping STO layer to O_{ads}, resulting in a stronger O adsorption to the surface of the ultrathin heterostructure than on the pure STO surface. As discussed later, the enhanced OER activity quickly decreases with the thickness *n* (in u.c.) of the STO capping layer due to the diminishing electronic hybridization.

0.05 V (Extended Data Figure 7b). Atomic force microscopy images of electrode surface after OER confirms that they are atomically flat (Figure 2b). High-angle annular dark-field scanning transmission electron microscopy (HAADF STEM) in conjunction with energy-dispersive X-ray spectroscopy (EDX) is utilized to image the heterostructures that comprise of a number of SRO and STO layers with different thicknesses (Figure 2a, Extended Data Figure 10). Low-energy ion scattering (LEIS), employed as an independent and damage-free characterization, confirms the absence of Ru on the outermost surface of the heterostructure before (Extended

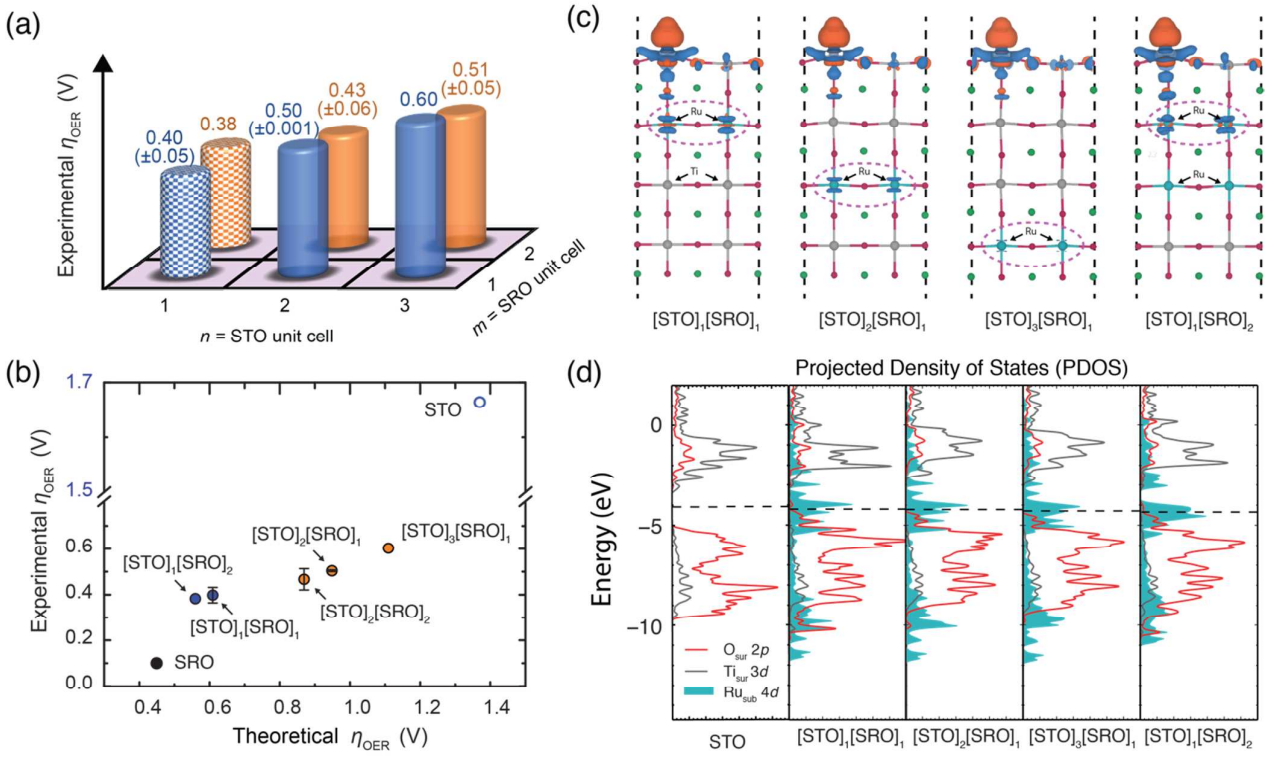

Figure 3. (a) Measured overpotentials at the current density of 2 μA/cm^2 for the $[STO]_n[SRO]_m$ heterostructures extracted from the cyclic voltammetry curves, as a function of the numbers of unit-cell layers *n* and *m* of STO and SRO in the heterostructure, respectively. For *n*=1 (bars with a "checkboard" fill) the samples have a convolution of the OER and dissolution currents. (b) Correlation between the theoretical and experimental (from CV at i = 2 μA/cm^2) values of overpotential. The overpotential for highly active SRO is taken at i = 100 μA/cm^2 and for inactive LTO_1/STO_{sub} at 80 nA/cm^2. The orange circles highlight stable catalysts, while blue circles represent the activities of unstable films derived from the first CV sweep (c) Calculated differential valence-electron charge densities of O_{ads} on $[STO]_n[SRO]_1$ (n=1,2, and 3) and $[STO]_1[SRO]_2$; charge depletion and accumulation are represented by blue and orange regions, respectively (isosurfaces are set to 0.005 e/Å^2). (d) DFT calculated projected density of states (PDOS) of the clean STO, $[STO]_n[SRO]_1$ (n =1, 2, and 3), and $[STO]_1[SRO]_2$ surfaces (for PDOS with O_{ads} see Extended Data Figure 5). Surface lattice oxygen 2*p*, surface Ti 3*d*, Ru 4*d* are plotted as red, grey solid lines and cyan filled lines, respectively. All energies are referenced to the vacuum level and the Fermi level for each system is indicated by a vertical black dashed line.

To validate our DFT predictions, we fabricated ultrathin $[STO]_n[SRO]_m$ heterostructures using pulsed-laser deposition (PLD) on atomically-flat (001) Nb-doped STO (0.5 wt.% doping), guided by *in situ* reflective high-energy electron diffraction (RHEED) (See Methods and Extended Data Figure 9). It is worth noting that there is no Nb in the capping STO layer, thus corresponding to the theoretical simulations. DFT estimates an upper bound of the influence from Nb dopants in the STO substrate on the surface OER overpotential to be less than

Data Figure 10) and after OER evaluation (Figure 2c). The extreme sensitivity of LEIS reveals surface impurities, which may not be visible by less sensitive characterization methods such as XPS. We hypothesize the impurities are due to low levels of contaminations in the electrolyte solution, which would likely affect the various electrodes employed in this study similarly. The dramatically different activity and stability among the heterostructured electrodes suggests that the impurity does not significantly influence the observed trend.

We characterized the OER activity of the ultrathin heterostructures as well as various baseline electrodes in 0.1 M KOH (pH= 12.8) using a rotating disk electrode setup. We confirm that bare Nb-doped STO single crystals show negligible current below 0.1 μA/cm^2 even at very high anodic potentials (>3 V *vs* RHE (Extended Data Figure 14). Although bulk SRO possesses good OER activity in both alkaline and acidic electrolytes, it also dissolves rapidly at the onset of OER.[4,7] Consistent with previous reports,[4,7,35] we observed that for 30-nm thick SRO on Nb-doped STO, OER and dissolution occurs simultaneously above ~1.2 V *vs* RHE (Extended Data Figures 12-13). For the $[STO]_n[SRO]_m$ heterostructures, we first assess bulk electronic transport using outer sphere fast redox couple $[Fe(CN)_6]^{3-/4-}$ (Figure 2d, solid lines). Significant current rectification was observed, which corresponds to the previously reported Schottky barrier between SRO and Nb-doped STO.[36,37] To eliminate the contribution from the Schottky barrier, we sintroduced a 1 u.c. of $LaTiO_3$ (LTO) dipole layer at the SRO/Nb:STO interface, inspired by the work of Yajima *et al.*[37] With this dipole layer in place, a reversible behavior of the $[Fe(CN)_6]^{3-/4-}$ couple was observed (Figure 2d, dashed lines). Our DFT calculations show that the theoretical OER overpotential is only slightly changed with the presence of the LTO layer (Extended Data Figure 3).

The OER activity and stability of a single unit-cell-thick SRO buried under STO ($[STO]_n[SRO]_1$ with n = 1-3), shown in Figure 2e and 2f alongside SRO and STO, confirm the sub-surface activation predicted by DFT. After 20 h of sustaining OER, $[STO]_2[SRO]_1$ exhibits a current density of 8 μA/cm^2 at an overpotential of 0.64 V vs RHE, whereas in SRO the current density became negligible (<1 μA/cm^2) within 3 min at the same overpotential. The modest current density in our heterostructures reflects the fact that the surface is atomically smooth (as evidenced by the step-terraced surface after reaction, Figure 2b), in contrast to other recent thin film systems studied such as $SrIrO_3$, which undergoes Sr leaching and significant surface roughening[10]. We compare the overpotentials at a current density of i = 2 μA/cm^2 (Figure 3a) for various n and m values. The overpotential (*vs* RHE) is 0.36 V, 0.48 V and 0.60 V for n = 1, 2, and 3, respectively. In most cases one unit-cell-thick STO was not enough to stabilize $[SRO]_1$, which is likely due to surface defects allowing electrolyte penetration to the SRO. As we increase the thickness of the surface STO layer from n=1 to 2, we observe a remarkable improvement in stability (Figure 2f). On the other hand, increasing the SRO thickness from m=1 to 2 does not significantly improve activity nor stability. We return to this important observation later. Thus, we demonstrate that a single u.c. of buried SRO activates STO oxide, which is located at the bottom of the DFT-predicted OER volcano (Figure 1c), and at the same time is stabilized by the STO capping layer at high anodic potentials for tens of hours.

To demonstrate reproducibility and for completeness, we also prepared $[STO]_n[SRO]_1$ (n=1-5, 7, 10) under slightly modified growth conditions (see Methods). We find that for n>5 the effective exchange current density (from the Tafel analysis) decreases rapidly with thickness of the STO capping layer, which is consistent with diminishing electronic influence of the sub-surface SRO, and the onset of electron-transport limitation.[30] (Extended Data Figure 20, 21). Interestingly, when $[STO]_{10}$ is directly grown on $[LTO]_1/STO_{sub}$, the film shows ~2 V higher overpotential than the $[STO]_{10}[SRO]_1$ heterostructure (Extended Data Figure 20), indicating that both LTO and SRO contribute the barrier-free band alignment across the interface with the Nb-doped STO substrate.

Computationally we find that the adsorbed O intermediate on any of the $[STO]_n[SRO]_m$ heterostructure surfaces has the same charge (Extended Data Table 1). However, the charge redistribution is spatially different (Figure 3c, and Extended Data Table 1) and depends strongly on the geometry of the heterostructure. For $[STO]_1[SRO]_1$ and $[STO]_1[SRO]_2$, most of the charge donated to the O adsorbate comes from the Ru sub-surface. In the case of $[STO]_1[SRO]_2$, all the charge comes from the 1st sub-surface Ru and almost none from the 2nd sub-surface Ru. Moreover, the involved Ru states of the $[STO]_1[SRO]_1$ and $[STO]_1[SRO]_2$ systems have the same energetic character, especially around the Fermi level, making the electronic hybridization between the oxygen and the surface of the $[STO]_1[SRO]_1$ and $[STO]_1[SRO]_2$ comparable to each other (Figure 3d). Hence, we conclude that 1 u.c. of sub-surface SRO is enough to activate the heterostructure and that Ru does not have to be directly part of the surface-active site, rather it can have an indirect multiple-nearest-neighbor effect on the reactivity. This result also highlights the minimum active material loading needed for OER.

The spatial proximity of the guest Ru sub-surface relative to the O adsorbate determines its ability to modify the surface reactivity. The deeper buried the Ru layer is, the more diminishing is its influence, as would be expected intuitively. This is evidenced by the charge donated by the Ru that propagates to the adsorbate (Figure 3c) through the hybridization with the STO capping layers. Importantly, in all of the $[STO]_n[SRO]_1$ examined, the guest Ru states of the SRO sub-surface are energetically positioned at the Fermi level (Figure 3d, Extended Data Figure 4-5). However, they are not all spatially accessible to directly hybridize with the oxygen adsorbate. In general, systems with a large number of states at the Fermi level will be less stable if these unsaturated bonds are exposed to the electrolyte[4]. In other words, there is a clear trade-off between activity and stability. For all $[STO]_n[SRO]_1$ systems, the bonding states of the adsorbed O (Extended Data Figure 5) are positioned at the same energy relative to the Fermi level and hence have the same filling in agreement with the Bader charge analysis. Therefore, it is the number of electrons transferred from the sub-surface Ru to the adsorbed O that leads to the difference in O binding energy with different capping STO thickness. Because of the linear correlation between the adsorption energies of OH^* and O^* (a slope of ~0.5 for the $[STO]_n[SRO]_m$ system, (Extended Data

Figure 6), a weaker oxygen binding leads to a larger ΔG_{O^*}-ΔG_{OH^*} and, hence, results in a lower OER activity. Taken together, there are two main effects governing the reactivity and enhancing the bonding: the energetic position of the sub-surface guest states in the host material and the spatial accessibility of these states to the adsorbate. Hence, the activation mechanism in these oxide heterostructures is uniquely different from the metallic near-surface alloys, where the reactivity is only perturbed by the guest metallic state,[38] while here the introduction of the guest metal oxide introduces states with completely new character not present in the original host material.

The overall trends with respect to *n* and *m* agree between our theoretical and experimental findings with better agreement for small n-values (Figure 3b). Bulk STO, also shown, deviates from this agreement because electron tunneling is rate-limiting. Minor inter-diffusion of ions between the layers of the heterostructures, incomplete mitigation of the Schottky barrier (residual space-charge region), and existence of oxygen vacancies (see Extended Data Figure 7), are other factors that could contribute to the deviation between theory and experiment.

Conclusions

In summary, we demonstrated a model system for studying complex oxides with a multi-core-shell-like architecture for electrochemical water oxidation, which consists of an inactive core with an extremely low amount of active SRO covering the core and a capping (protecting) STO shell. As little as one u.c. of SRO can activate an OER-inert STO if buried as a sub-surface layer with no Ru at the adsorption site, while as little as two u.c. of STO can protect SRO from dissolution. Our first-principles calculations show that the same mechanism for activation of an OER-inert STO by a subsurface OER-active layer can be generalized to other $SrMO_3$ sub-surface layers as well as other host oxides.[39] We note that translating our results to core-shell nanoparticles requires further work, especially on current collection. Finally, our study provides the insight into the role of unit-cell level modification of the surface and subsurface layers of oxide electrocatalysts, opening up a rich playground for further discovery and design of active and stable heterostructured materials.

Methods

First-principles calculations. Spin-polarized DFT calculations were performed using Quantum ESPRESSO[40] in combination with Atomic Simulation Environment.[41] Core electrons were described using ultrashort pseudopotentials.[42] Kohn-Sham wave functions were expanded in a plane-wave basis with a kinetic energy cutoff of 500 eV. The exchange-correlation energy was evaluated by the generalized gradient approximation (GGA) using the Perdew-Burke-Ernzerhof (PBE) functional.[43] All geometries were considered optimized with the force on each atom was < 0.01 eV/Å. The heterostructure surfaces were modeled with a 5-layer thick (2×2) $SrTiO_3$ slab exposing the (100) facet with different number of sub-surface layer(s) substituted by SRO. In other words, the SRO layer is lattice-matched to the STO lattice mimicking the epitaxial growth condition in experiments. The bottom two STO layers of the slab were fixed in their bulk positions, while the rest of the system was allowed to relax. A vacuum spacing of 14 Å was added to all supercell models to separate the slabs and avoid interaction between periodic images. A (4×4×1) Monkhorst-Pack *k*-point grid was used for Brillouin-zone sampling.[44] The intermediates were modeled with an adsorbate coverage of 1/4ML relative to the surface Ti atoms. Bader charge analysis was used to decompose the charge density into volumes around each atom.[45,46]

Thin film preparation and characterization. All thin film samples were grown by pulsed-laser deposition (PLD/MBE 2300, PVD Products) on 10x10 mm^2 (001) Nb-doped $SrTiO_3$ (0.5 wt.% doping) (Shinkosha Co., Japan). The growth temperature was 620-650 °C under oxygen pressure of 0.3-1 mTorr. The target-to-substrate distance was 84 mm, the laser fluence was 1 J/cm^2. After each deposition, the film was cooled down under 200 mTorr of oxygen. Prior to the growth of ultrathin heterostructures ($[STO]_m[SRO]_n$/LTO), the Nb-doped $SrTiO_3$ substrates for were first etched in the buffered HF (pH = 4.5) and then annealed at 1000 °C for 2 h. An in-lab sintered $SrTiO_3$ (99.9% $SrCO_3$, 99.9% TiO_2), $LaTiO_3$ (99.99% La_2O_3, 99.9% TiO_2 purity) and commercial $SrRuO_3$ (80% density, 99.95% elemental purity; Toshima Manufacturing Co.) ceramic pellets were used for laser ablation. The growth of ultrathin heterostructures was monitored in situ using a RHEED system (TorrRHEED™, Staib Instruments) operated at 35 kV (1.5 μA). Under the first deposition condition, the plume off-axis angle was set to ~15-20°, while for the second conditions it was 0°. Prior to the growth of the heterostructure, on each substrate one unit cell (or less) of STO was grown to restore the surface from possible inhomogeneities and smooth terrace steps; the growth stopped upon maximization of the RHEED intensity.

X-ray diffraction and X-ray reflectivity of thicker films were collected using PANalytical X'Pert PRO diffractometer equipped with a double monochromator and operating in a parallel-beam geometry. Atomic force microscopy was carried out on the NX-10 SPM system (Park Systems) in a contact mode using Si SPM tips (< 7 nm tip radius, PPP-CONTR, Nanosensors™). Low-energy ion scattering was performed on thin films using ION-TOF Qtac^{100} High-Resolution LEIS spectrometer with either 3 keV He^+ (5x10^{14} ions/cm^2) or 5 keV Ne^+ (2x10^{14} ions/cm^2) primary ions beams (3000 eV pass energy). This system causes only minor damage to the surface when compared to traditional LEIS instruments. Prior to the spectra acquisition, the samples were treated in atomic oxygen for 10 mins (unless specified otherwise) at room temperature to clean the surface. During LEIS measurements, the beam was rastering over the surface in the middle of the sample to avoid prolong exposure to ions, the spot size was

1500x1500 μm^2. For depth profiling 5 keV Ne^+ was used for spectra acquisition and 0.5 keV Ar^+ (10^{15} ions·cm^{-2}·cyc^{-1}) for sputtering. Specimen preparation for TEM was performed by mechanical polishing and dimpling, followed by the ion milling (Gatan PIPS II ion mill). HAADF-STEM images were acquired in the double aberration corrected FEI Titan Cubed Themis^3 TEM operated at 200 kV. Mapping of chemical elements (Energy-dispersive X-ray spectroscopy) was carried out with the SuperEDX Si drift detector (FEI). Electron energy loss spectroscopy (EELS) analysis and mapping was done using the Gatan Quantum ERS GIF spectrometer. The images were filtered using a Wiener filter. We found that acquisition of high-quality TEM data requires significant optimization of the TEM specimen preparation procedure and imaging conditions. The optimized acquisition parameters for EELS (energy dispersion 0.25-0.5 eV/ch) and EDX maps are as follows: current is ~150 pA, total acquisition time is ~5 min, camera length is 29.5 mm.

Electrochemical characterization. To perform electrochemical experiments on thin-film samples, we implemented a home-built holder for the 10x10 mm^2 flat samples into the rotating disk electrode (RDE, Pine Research). The substrate was tight-contacted from the bottom using conductive carbon paste to the glassy carbon disk insert (Pine Research). In order to eliminate the Schottky barrier between the Nb-doped $SrTiO_3$ and glassy carbon, a 10-nm layer of Ti was first deposited on the back of the substrate, followed by deposition of a thick (100-200 nm) Pt layer. On the film side, the area exposed to the electrolyte was 0.5 mm^2 as defined by the *o*-ring (nitrile, O-rings Inc.) in the home-built holder. The RDE shaft was rotating at 1000 rpm, yet no significant dependence of the OER current on rotation rate was observed above 500 rpm. Electrochemical testing was performed using BioLogic VSP-300 potentiostat, in the 175-mL alkaline-resistant Teflon cell (Pine Research) with a Pt wire as a counter electrode. Electrical impedance spectroscopy (EIS) was conducted with the amplitude of 10 mV (open circuit) and, the correction for the cell resistance (typically, 80-150 Ω) was made based on the high-frequency intercept of the real impedance. The electrolyte solution of 0.1 M KOH, prepared by dissolving KOH pellets (Sigma-Aldrich, 99.99%) in deionized water (Millipore, >18.2 MΩcm), was O_2-saturated prior to testing for at least 30 minutes and maintained under O_2 atmosphere during testing. Potentials were referenced to either leakless Ag/AgCl (miniature, EDAQ, model ET072) or Hg/HgO (CHI Instruments). Both reference electrodes were periodically calibrated to the real reversible hydrogen electrode (HydroFlex) in 0.1 M KOH. For $[Fe(CN)_6]^{3+/4+}$ measurements the solutions of 20 mM $K_3Fe(CN)_6$ (Sigma-Aldrich, 99%) and 20 mM $K_4Fe(CN)_6{\cdot}3H_2O$ (Sigma-Aldrich, 99.99%) were prepared in the Ar-saturated 0.1 M KOH electrolyte and cyclic voltammetry was performed without rotating the electrode.

Conflicts of interest

There are no conflicts to declare.

Acknowledgements

This work was supported by the Department of Energy, Office of Basic Energy Sciences, Division of Materials Sciences and Engineering (contract no. DE-AC02-76SF00515). A.V. acknowledges the Canadian Institute for Advanced Research (CIFAR) for support through the Bio-inspired Solar Energy Program. B.B. acknowledges financial support by the German Research Foundation (DFG) under grant no. BU 2875/2-1. The authors acknowledge the use of the computer time allocation at the National Energy Research Scientific Computing Center (NERSC), a DOE Office of Science User Facility supported by the Office of Science of the U.S. Department of Energy under Contract No. DE-AC02-05CH1123, and the Extreme Science and Engineering Discovery Environment (XSEDE) supported through National Science Foundation Energy under Award Number CHE160084. TEM characterization was carried out at the Hewlett Packard Labs. We thank Jiaming Zhang for numerous discussion and letting us use the microscope. We also thank Madhur Boloor, Yiyang Li and Tianchi Liu for the help with the back contact preparation, and Liming Zhang for useful discussions.

References

1. Seh, Z.W. *et al.* Combining theory and experiment in electrocatalysis: Insights into materials design. *Science* **355** (2017).
2. Stamenkovic, V.R., Strmcnik, D., Lopes, P.P. & Markovic, N.M. Energy and fuels from electrochemical interfaces. *Nat Mater* **16**, 57-69 (2017).
3. Hong, W.T. *et al.* Toward the rational design of non-precious transition metal oxides for oxygen electrocatalysis. *Energy & Environmental Science* **8**, 1404-1427 (2015).
4. Chang, S.H. *et al.* Functional links between stability and reactivity of strontium ruthenate single crystals during oxygen evolution. *Nature Communications* **5**, 4191 (2014).
5. Cherevko, S. *et al.* Dissolution of Noble Metals during Oxygen Evolution in Acidic Media. *ChemCatChem* **6**, 2219-2223 (2014).
6. Danilovic, N. *et al.* Activity–Stability Trends for the Oxygen Evolution Reaction on Monometallic Oxides in Acidic Environments. *The Journal of Physical Chemistry Letters* **5**, 2474-2478 (2014).
7. Kim, B.-J. *et al.* Unraveling Thermodynamics, Stability, and Oxygen Evolution Activity of Strontium Ruthenium Perovskite Oxide. *ACS Catalysis* **7**, 3245-3256 (2017).
8. Sangle, A.L. *et al.* Very High Surface Area Mesoporous Thin Films of $SrTiO_3$ Grown by Pulsed Laser Deposition and Application to Efficient Photoelectrochemical Water Splitting. *Nano Letters* **16**, 7338-7345 (2016).
9. Gawande, M.B. *et al.* Core-shell nanoparticles: synthesis and applications in catalysis and electrocatalysis. *Chemical Society Reviews* **44**, 7540-7590 (2015).
10. Seitz, L.C. *et al.* A highly active and stable $IrO_x/SrIrO_3$ catalyst for the oxygen evolution reaction. *Science* **353**, 1011-1014 (2016).
11. May, K.J. *et al.* Influence of Oxygen Evolution during Water Oxidation on the Surface of Perovskite Oxide Catalysts. *The Journal of Physical Chemistry Letters* **3**, 3264-3270 (2012).

12. Anderson, R.M. *et al.* A Theoretical and Experimental Approach for Correlating Nanoparticle Structure and Electrocatalytic Activity. *Accounts of Chemical Research* **48**, 1351-1357 (2015).
13. Strasser, P. Free Electrons to Molecular Bonds and Back: Closing the Energetic Oxygen Reduction (ORR)–Oxygen Evolution (OER) Cycle Using Core–Shell Nanoelectrocatalysts. *Accounts of Chemical Research* **49**, 2658-2668 (2016).
14. Wang, C. *et al.* Design and Synthesis of Bimetallic Electrocatalyst with Multilayered Pt-Skin Surfaces. *Journal of the American Chemical Society* **133**, 14396-14403 (2011).
15. Zhou, W.-P. *et al.* Improving Electrocatalysts for O_2 Reduction by Fine-Tuning the Pt−Support Interaction: Pt Monolayer on the Surfaces of a $Pd_3Fe(111)$ Single-Crystal Alloy. *Journal of the American Chemical Society* **131**, 12755-12762 (2009).
16. Strasser, P. *et al.* Lattice-strain control of the activity in dealloyed core–shell fuel cell catalysts. *Nat Chem* **2**, 454-460 (2010).
17. Ghosh Chaudhuri, R. & Paria, S. Core/Shell Nanoparticles: Classes, Properties, Synthesis Mechanisms, Characterization, and Applications. *Chemical Reviews* **112**, 2373-2433 (2012).
18. Zhang, Q., Lee, I., Joo, J.B., Zaera, F. & Yin, Y. Core–Shell Nanostructured Catalysts. *Accounts of Chemical Research* **46**, 1816-1824 (2013).
19. Lebedev, D. *et al.* Highly Active and Stable Iridium Pyrochlores for Oxygen Evolution Reaction. *Chemistry of Materials* **29**, 5182-5191 (2017).
20. Petrie, J.R., Jeen, H., Barron, S.C., Meyer, T.L. & Lee, H.N. Enhancing Perovskite Electrocatalysis through Strain Tuning of the Oxygen Deficiency. *Journal of the American Chemical Society* **138**, 7252-7255 (2016).
21. Tang, R. *et al.* Oxygen evolution reaction electrocatalysis on $SrIrO_3$ grown using molecular beam epitaxy. *Journal of Materials Chemistry A* **4**, 6831-6836 (2016).
22. Stoerzinger, K.A., Qiao, L., Biegalski, M.D. & Shao-Horn, Y. Orientation-Dependent Oxygen Evolution Activities of Rutile IrO_2 and RuO_2. *The Journal of Physical Chemistry Letters* **5**, 1636-1641 (2014).
23. Stoerzinger, K.A. *et al.* Orientation-Dependent Oxygen Evolution on RuO_2 without Lattice Exchange. *ACS Energy Letters* **2**, 876-881 (2017).
24. Stoerzinger, K.A., Choi, W.S., Jeen, H., Lee, H.N. & Shao-Horn, Y. Role of Strain and Conductivity in Oxygen Electrocatalysis on $LaCoO_3$ Thin Films. *The Journal of Physical Chemistry Letters* **6**, 487-492 (2015).
25. Lee, S.A. *et al.* Enhanced electrocatalytic activity via phase transitions in strongly correlated $SrRuO_3$ thin films. *Energy & Environmental Science* **10**, 924-930 (2017).
26. Scholz, J. *et al.* Rotating Ring–Disk Electrode Study of Oxygen Evolution at a Perovskite Surface: Correlating Activity to Manganese Concentration. *The Journal of Physical Chemistry C* **120**, 27746-27756 (2016).
27. Abild-Pedersen, F. *et al.* Scaling Properties of Adsorption Energies for Hydrogen-Containing Molecules on Transition-Metal Surfaces. *Physical Review Letters* **99**, 016105 (2007).
28. Baiutti, F. *et al.* High-temperature superconductivity in space-charge regions of lanthanum cuprate induced by two-dimensional doping. *Nature Communications* **6**, 8586 (2015).
29. Scheuermann, A.G., Prange, J.D., Gunji, M., Chidsey, C.E.D. & McIntyre, P.C. Effects of catalyst material and atomic layer deposited TiO_2 oxide thickness on the water oxidation performance of metal-insulator-silicon anodes. *Energy & Environmental Science* **6**, 2487-2496 (2013).
30. Viswanathan, V., Pickrahn, K.L., Luntz, A.C., Bent, S.F. & Nørskov, J.K. Nanoscale Limitations in Metal Oxide Electrocatalysts for Oxygen Evolution. *Nano Letters* **14**, 5853-5857 (2014).
31. Rong, X., Parolin, J. & Kolpak, A.M. A Fundamental Relationship between Reaction Mechanism and Stability in Metal Oxide Catalysts for Oxygen Evolution. *ACS Catalysis* **6**, 1153-1158 (2016).
32. Mefford, J.T. *et al.* Water electrolysis on $La_{1-x}Sr_xCoO_{3-\delta}$ perovskite electrocatalysts. **7**, 11053 (2016).
33. Man, I.C. *et al.* Universality in Oxygen Evolution Electrocatalysis on Oxide Surfaces. *ChemCatChem* **3**, 1159-1165 (2011).
34. Rossmeisl, J., Logadottir, A. & Nørskov, J.K. Electrolysis of water on (oxidized) metal surfaces. *Chemical Physics* **319**, 178-184 (2005).
35. Chang, S.H. *et al.* Activity-stability relationship in the surface electrochemistry of the oxygen evolution reaction. *Faraday Discussions* **176**, 125-133 (2014).
36. Hikita, Y., Kozuka, Y., Susaki, T., Takagi, H. & Hwang, H.Y. Characterization of the Schottky barrier in $SrRuO_3$ / $Nb:SrTiO_3$ junctions. *Applied Physics Letters* **90**, 143507 (2007).
37. Yajima, T. *et al.* Controlling band alignments by artificial interface dipoles at perovskite heterointerfaces. *Nature Communications* **6**, 6759 (2015).
38. Greeley, J. & Mavrikakis, M. Alloy catalysts designed from first principles. *Nature Materials* **3**, 810 (2004).
39. L. Zhang, A.S. Raman & Vojvodic, A. Oxide heterostructures for water splitting. *In preparation* (2017).
40. Paolo, G. *et al.* QUANTUM ESPRESSO: a modular and open-source software project for quantum simulations of materials. *Journal of Physics: Condensed Matter* **21**, 395502 (2009).
41. Ask Hjorth, L. *et al.* The atomic simulation environment — a Python library for working with atoms. *Journal of Physics: Condensed Matter* **29**, 273002 (2017).
42. Vanderbilt, D. Soft self-consistent pseudopotentials in a generalized eigenvalue formalism. *Physical Review B* **41**, 7892-7895 (1990).
43. Perdew, J.P., Burke, K. & Ernzerhof, M. Generalized Gradient Approximation Made Simple. *Physical Review Letters* **77**, 3865-3868 (1996).
44. Monkhorst, H.J. & Pack, J.D. Special points for Brillouin-zone integrations. *Physical Review B* **13**, 5188-5192 (1976).
45. Bader, R.F.W. *Atoms in Molecules: A Quantum Theory*. (Clarendon Press, 1994).
46. Tang, W., Sanville, E. & Henkelman, G. A grid-based Bader analysis algorithm without lattice bias. *Journal of Physics: Condensed Matter* **21**, 084204 (2009).

1